Local control of microstructure and mechanical properties of high-strength steel in electric arc-based additive manufacturing

Babu, Aravind; Ebrahimi, Amin; Wu, K.; Richardson, Ian M.; Hermans, Marcel J.M.

DOI
10.1016/j.jmrt.2023.07.262

Publication date
2023

Document Version
Final published version

Published in
Journal of Materials Research and Technology

Citation (APA)
Babu, A., Ebrahimi, A., Wu, K., Richardson, I. M., & Hermans, M. J. M. (2023). Local control of microstructure and mechanical properties of high-strength steel in electric arc-based additive manufacturing. *Journal of Materials Research and Technology*, *26*, 1508-1526. https://doi.org/10.1016/j.jmrt.2023.07.262

JOURNAL OF MATERIALS RESEARCH AND TECHNOLOGY 2023;26:1508–1526

Available online at www.sciencedirect.com

jmr&t
Journal of Materials Research and Technology

journal homepage: www.elsevier.com/locate/jmrt

Local control of microstructure and mechanical properties of high-strength steel in electric arc-based additive manufacturing

Aravind Babu[*], *Amin Ebrahimi, Kuo-Hao Wu, Ian M. Richardson, Marcel J.M. Hermans*

Department of Materials Science and Engineering, Faculty of Mechanical, Maritime and Materials Engineering, Delft University of Technology, 2628CD Delft, the Netherlands

ARTICLE INFO

Article history:
Received 6 June 2023
Accepted 29 July 2023
Available online 3 August 2023

Keywords:
Metal additive manufacturing
Wire arc additive manufacturing (WAAM)
Microstructural control
Mechanical behaviour
High-strength steel
Thermal modelling

ABSTRACT

Additive manufacturing offers a significant potential for producing metallic parts with distinctly localised microstructures and mechanical properties, commonly known as functional grading. While functional grading is generally accomplished through compositional variations or in-situ thermo-mechanical treatments, variation of process parameters during additive manufacturing can offer a promising alternative approach. Focusing on the electric arc-based additive manufacturing process, this work focuses on the functional grading of high-strength steel (S690 grade) by adjusting the travel speed and inter-pass temperature. Through a combination of thermal simulations and experimental measurements on single bead-on-plate depositions, it is shown that the microstructure and the mechanical properties of parts can be controlled through the rational adjustment of process parameters. A rectangular block was fabricated to demonstrate functional grading using a constant wire feed rate and varying travel speed. The rectangular block consisted of a low heat input (LHI) region deposited between high heat input (HHI) zones. A graded microstructure was obtained with the HHI zones composed of a mixture of polygonal ferrite, acicular ferrite, and bainite, while the LHI region was primarily composed of martensite. The hardness and profilometry-based indentation plastometry measurements indicated that the LHI region exhibited higher hardness (32%) and strength (50%), but lower uniform elongation (80%), compared to the HHI zones. The present study demonstrates the potential to achieve functional grading by adjusting process parameters in electric arc-based additive manufacturing, providing opportunities for tailor-made properties in parts.

1. Introduction

Additive manufacturing (AM), also known as 3D printing, is an advanced manufacturing technique that produces near-net-shape parts layer-by-layer and offers the prospect of revolutionising the design, manufacturing and repair of products in various industries, such as aerospace, maritime and automotive. In contrast to conventional manufacturing

---

[*] Corresponding author.

E-mail addresses: A.Babu@tudelft.nl (A. Babu), A.Ebrahimi@tudelft.nl (A. Ebrahimi), M.J.M.Hermans@tudelft.nl (M.J.M. Hermans).

https://doi.org/10.1016/j.jmrt.2023.07.262

Nomenclature:

η	Process efficiency
ε	Radiation emissivity
α_γ	Lattice constant of austenite (Å)
C_γ	Carbon concentration in austenite (wt%)
V_t	Travel speed (mm s^{-1})
Ac_3	Upper critical temperature (°C)
Ac_1	Lower critical temperature (°C)
M_s	Martensite start temperature (°C)
M_f	Martensite finish temperature (°C)
R	Solidification velocity (m s^{-1})
G	Temperature gradient ($^\circ\text{C m}^{-1}$)
a_f	Front ellipsoidal length (mm)
a_r	Rear ellipsoidal length (mm)
b	Half-width of the melt pool (mm)
d	Depth of the melt pool (mm)
f_f	Front power distribution factor
f_r	Rear power distribution factor
h_c	Heat transfer coefficient ($\text{W m}^{-2}\text{ K}^{-1}$)
q_i	Linear heat input (J mm^{-1})
M	Gaussian parameter
AM	Additive manufacturing
WAAM	Wire arc additive manufacturing
LHI	Low heat input
HHI	High heat input
PIP	Profilometry-based indentation plastometry
CTWD	Contact tip to workpiece distance (mm)
XRD	X-Ray diffraction
RA	Retained austenite
CCT	Continuous cooling transformation
HAZ	Heat affected zone
SEM	Scanning electron microscopy
PAG	Prior austenite grain
BCC	Body-centered cubic
BCT	Body-centered tetragonal
MA	Martensite austenite
ICHAZ	Inter-critical heat-affected zone
HSLA	High strength low alloy
YS	Yield strength (MPa)
UTS	Ultimate tensile strength (MPa)

techniques, additive manufacturing stands out due to its high degree of customization, manufacturing flexibility and incorporation of intricate deposition features. The wire arc additive manufacturing (WAAM) process, involves supplying material, in the form of wire into a zone heated by an arc heat source and depositing the resulting molten material along a predetermined path, commonly derived from a computer-aided design (CAD) file [1]. WAAM is suitable for building large-volume parts with dimensions over a cubic meter, due to the high deposition rates and manufacturing efficiencies achievable [1–3]. Arc welding processes applied in additive manufacturing are typically gas tungsten arc welding (GTAW), plasma arc welding (PAW) and gas metal arc welding (GMAW) [3]. Compared to GTAW and PAW-based AM, GMAW is often preferred in practice since the deposited material is supplied coaxially from the welding torch, eliminating the need for an external wire feeder, and thus simplifying toolpath planning. Moreover, the deposition rate is generally higher than that of GTAW and PAW [3]. GMAW-based AM offers high deposition rates (typically 1–10 kg h^{-1}), low material wastage and high process efficiency (in the order of 90%). It also offers significant potential for local compositional and microstructural control (also known as functional grading) [3–6].

Previous studies have shown that the microstructures and mechanical properties of parts built using wire arc additive manufacturing differ considerably from those built by conventional manufacturing techniques (*e.g.* casting or forging) [3]. Such differences are partially ascribed to the localised heating and cooling cycles during WAAM [7]. Changes in process parameters, as well as continuous changes of the bulk metal geometry during printing, affect the process behaviour [8–13] and local thermal profiles [14–16]. A large body of literature exists explaining the effects of process parameters on the properties of additively manufactured metallic parts (see for instance Refs. [7,17–20]). Duarte *et al.* [17] manufactured thin wall structures using continuous and pulsed welding modes and showed that the micro-hardness and tensile strength of high-strength low-alloy steel (ER110S-G) increase with decreasing heat input. They attributed this observation to the formation of non-equilibrium phases such as bainite and martensite at low heat inputs. Rodideal *et al.* [18] extended the previous studies on the effect of heat input on mechanical properties fabricated with high-strength low-alloy steel (ER110S-G) to thick walls and confirmed the negative correlation of heat input with hardness and tensile strength. Following a similar approach, Panchenko *et al.* [21] controlled heat input in GMAW-based AM using two different metal transfer modes and confirmed that changing heat input can affect the microstructure evolution of high-strength low-alloy steel (ER110S-G) blocks. The published research confirms the role of heat input in controlling microstructure and properties in WAAM parts. Heat input to the material in WAAM can be controlled by the changing travel speed, wire feed rate or welding current. Changing heat input in WAAM not only affects the final properties of the printed parts but also results in changes in the bead geometry and dimension [17,22].

A broad range of metallic materials, such as nickel alloys, titanium alloys, aluminium alloys and steel, has been used in wire-arc additive manufacturing [23]. Recent trends in WAAM research indicate significant interest in printing steel parts due to their numerous industrial applications. In the present study, test cuboids are additively manufactured using a high-strength steel alloy (S690). High-strength steels are widely used for structural applications due to their relatively high yield strength (greater than 460 MPa) and elongation at fracture of about 20% [24]. Moreover, high-strength steels generally contain low amounts of carbon (0.05 and 0.25 wt%) in their composition, improving their weldability, formability, and resistance to corrosion. Solid-state phase transformations in steels during WAAM lead to the decomposition of austenite to different phases, such as grain boundary ferrite, bainite, acicular ferrite and martensite [25]. Individual phase fractions of each of these transformation products affect the mechanical properties of the part produced [25–27]. Phase fractions during austenite decomposition depend on the peak temperature of the thermal profile and the cooling rate [28,29]. Thus, there is a possibility to control solid-state phase transformations in WAAM by changing inter-pass temperature, by altering the dwell time or using auxiliary cooling mechanisms [30–32].

A survey of the literature indicates that the majority of publications on wire arc additive manufacturing focus on the fabrication of walls and blocks with a single set of process parameters. Further studies are required to unleash the potential of tailor-made site-specific properties. Changing process parameters affects the resulting thermal cycles and can influence metallurgical phenomena such as solidification, solid-state phase transformation and tempering, leading to changes in the final microstructure and properties [33]. Applications of such a tailored microstructure can have implications on part design to achieve enhanced wear, scratch, or impact resistance in specific regions while maintaining toughness or ductility in the other regions. Moreover, the transition in microstructure and local properties can facilitate stress redistribution within the material, when subjected to external loads. Tailoring the microstructure of an ER110S-G steel part remains relatively unexplored, especially in relation to altering the heat input during fabrication. Previous attempts to functionally grade ER110S-G steels were limited to the use of corrosion resistant alloys and different metal transfer modes [21]. Rodrigues *et al.* [34] combined ER110S-G steel with a copper-based alloy to improve heat extraction, fatigue and wear resistance in addition to corrosion resistance. However, such an approach can cause a mismatch in material properties, leading to potential issues such as cracking, the formation of brittle compounds and reduced strength. Panchenko *et al.* [21] fabricated a graded structure with ER110S-G steel by modulating heat input, although the graded structure was limited to the case study of a single layer, limiting its applicability to multi-layer cases. Additionally, deposition of the graded part relied on a specialized power source (CMT) leading to higher investment and cost and complexity in maintenance. By controlling the heat input in wire arc additive manufacturing through the manipulation of travel speed, wire feed rate or welding current, it becomes possible to achieve the desired properties without the need for specialized power sources, complex cooling mechanisms, or compositional variations that may introduce unwanted complexities. Such a simple methodology to produce tailored microstructures and properties facilitates the optimisation of part designs to meet material performance requirements in specific regions of the manufactured components.

The objective of the present work is to locally control the microstructure and mechanical properties (*i.e.* functional grading) of a high-strength steel alloy (S690) in wire arc additive manufacturing by adjusting heat input and inter-pass temperature. It can be hypothesized that with a decrease in heat input and interpass temperature, higher martensite phase fractions, hardness, and material strength can be attained. Heat input during the process was controlled by changing the travel speed. Numerical simulations based on a finite-element method were developed to predict thermal profiles during WAAM. A test cuboid was additively manufactured, and microstructural characterisation and microhardness measurements were performed on samples extracted from the deposited block. Additionally, to determine the local yield and ultimate tensile strengths of the constructed parts, measurements were carried out using the profilometry-based indentation plastometry (PIP) technique. The microstructural evolution in different regions and the corresponding mechanical properties are discussed in detail. The results of the present study contribute to our understanding of microstructure control and mechanical property tailoring in WAAM of high-strength steel alloys.

2. Methods

2.1. *Experimental setup and procedure*

Single bead-on-plate depositions with a length of 120 mm were made using different travel speeds ranging from 5 mm s^{-1} to 20 mm s^{-1} on a substrate with dimensions of 140 × 50 × 10 mm^3. The beads were visually inspected for possible defects, such as humping and lack of fusion. A rectangular block with dimensions of 125 × 21 × 23 mm^3 was then produced using multiple sets of process parameters to locally control the microstructure and mechanical properties, as shown schematically in Fig. 1. Functional grading of properties in the blocks was achieved by varying the travel speed, and the process parameters were selected based on the results of the single bead-on-plate evaluations.

The block shown in Fig. 1(b) comprises two regions, one produced using a low heat input (LHI) and the other using a high heat input (HHI). The HHI regions were produced by depositing three horizontal overlapping beads and three vertical layers. The LHI region was produced by depositing six layers comprised of six overlapping beads. The HHI regions were deposited with an inter-pass temperature of 100 °C and the LHI region with an inter-pass temperature of 50 °C. A lower interpass temperature was chosen to enhance the cooling rates in the LHI region. The hatch spacing (p) was selected to be 2/3 (two thirds) of the bead width, as determined from the single bead-on-plate experiments, to minimise surface waviness [35].

A multi-axis Fanuc robot was used to control the torch's movement and a Fronius CMT 5000i supplied the electric power. The distance between the contact tip and the workpiece (CTWD) was set to 15 mm and the wire feed rate was fixed at 6 m min^{-1}. A pulsed mode droplet transfer was chosen to conduct experiments to reduce total heat input and spatter formation [36]. A bidirectional scanning strategy was employed to manufacture the block. The substrate material was S255 carbon steel, and its temperature before the deposition commenced was 20 °C. Protegon (85% Ar + 15% CO_2) was employed as shielding gas with a flow rate of 19 L min^{-1}. A high-strength steel (Lincoln Electric-LNM MoNiVa) wire with a diameter of 1.2 mm was employed as the wire feedstock material. The nominal composition of the high-strength steel filler wire is given in Table 1. The wire has a yield strength (as-deposited) of greater than 690 MPa.

Voltage and current were measured during deposition using a Triton 4000 data acquisition system at a frequency of 5 kHz. The linear heat input (q_l) during deposition is estimated

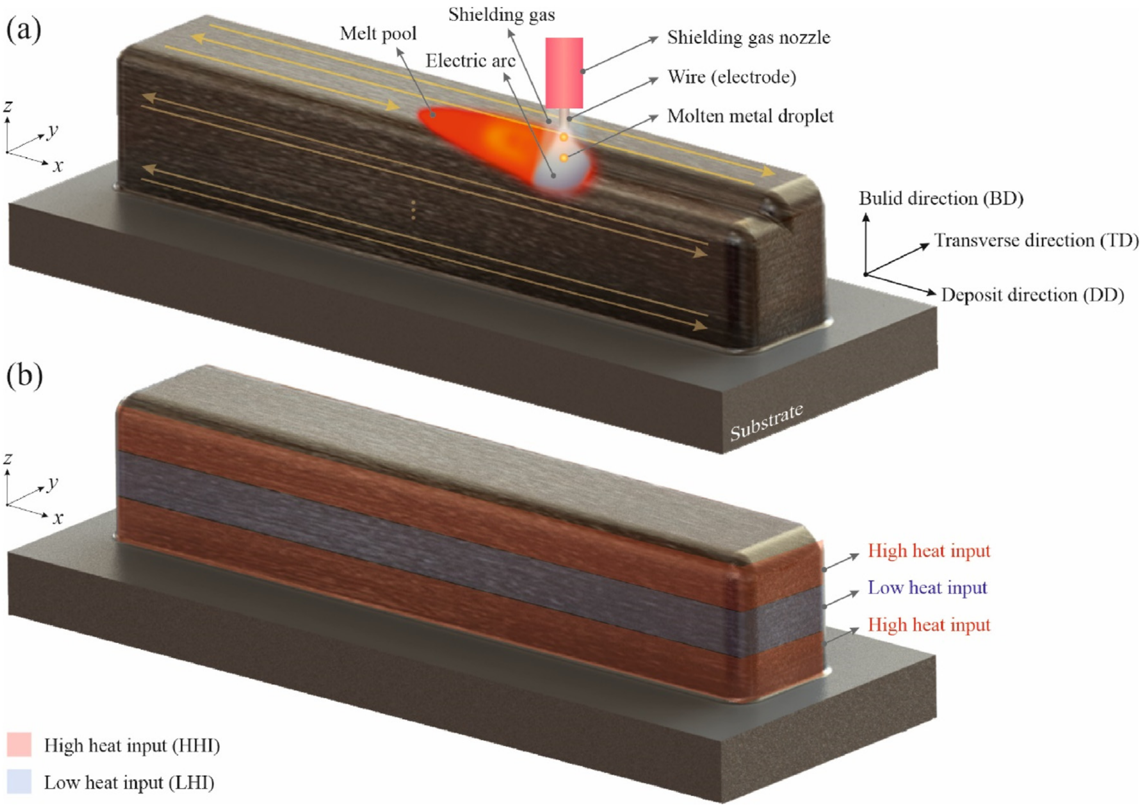

Fig. 1 – (a) Schematic of electric arc-based additive manufacturing process, commonly referred to as wire-arc additive manufacturing (WAAM). (b) Illustration of high and low heat input regions in the deposited rectangular block. Yellow arrows on the block indicate the bidirectional printing strategy.

based on measured instantaneous current and voltage values as follows:

$$q_i = \frac{\eta \sum_{i=0}^{n} \frac{U_i I_i}{n}}{V_t}, \qquad (1)$$

where U_i is the voltage, I_i is the current, V_t is the travel speed and η the process efficiency. The peak current, base current and pulse frequency were extracted from the current-voltage waveform and were approximately 532 A, 48 A and 140 Hz respectively. A digital thermometer (Voltcraft PL-125-T4USB) was used to measure the substrate temperature and the interpass temperature. K-type thermocouples were positioned at two locations on the substrate in single bead-on-plate experiments for the bead deposited with a travel speed of 5 mm s^{-1}. The thermocouples were located in the middle of the substrate at 8 mm and 16 mm away from the centre line of the deposited bead. Thermal profiles from the thermocouples were recorded using a DL75 oscilloscope at a sampling rate of 200 Hz.

2.2. *Thermal modelling*

The microstructural evolution of deposited beads is contingent upon the thermal cycles to which the material is subjected. As such, knowledge regarding the evolution of thermal fields is crucial to gain a primary understanding of the potential for microstructural grading through variations in process parameters. A transient three-dimensional finite element model was constructed that solves the energy conservation equation to predict the evolution of the thermal field during and after material deposition. A double ellipsoidal volumetric heat source model [37] was adopted to describe the thermal energy input from the electric arc. The parameters required to define the heat source model are presented in Table 2. Heat losses from the part due to convection and radiation were accounted for in the simulations by defining appropriate boundary conditions. The radiation emissivity (ε) and the heat transfer coefficient (h_c) were set to 0.8 and 15 W m^{-2} K^{-1} respectively, and the ambient temperature was equal to 25 °C. Temperature-dependent material properties were used in the

Table 1 – Nominal composition of the high-strength steel (Lincoln Electric LNM MoNiVa) wire used as the wire feedstock material in the experiments as provided by the supplier.

Constituent	C	Mn	Mo	Si	Ni	Cr	Cu	V	Fe
Composition (wt.%)	0.08	1.70	0.30	0.44	1.35	0.23	0.25	0.08	Balance

simulations, which were determined using the JMatPro software based on the material composition, as shown in Fig. 2. An apparent heat capacity model was employed in the simulations, which accounts for the latent heat of fusion by altering the specific heat capacity for the temperature range between the solidus and liquidus temperatures [38]. The solidus and liquidus temperatures, which are 1462 °C and 1509 °C respectively, were obtained from the thermodynamic database TCFE10 of the ThermoCalc software. Convection in the melt pool was modelled implicitly by artificially increasing the material thermal conductivity by a factor of 10 for temperatures above the liquidus temperature [39,40].

The bead geometry was idealised as a cuboid in the simulations, and its dimensions were extracted from experiments. A non-conformal mesh with uniform hexagonal elements was employed in the simulations. According to Goldak *et al.* [41], at least four elements are required to describe the double ellipsoidal heat source with adequate accuracy. After performing a grid independence test, a grid size of 2 mm in the substrate and 1 mm in the bead was chosen. An adaptive local mesh refinement was employed to refine the grid size for elements located inside and around the heat source and coarsen them when the temperature falls below 700 °C. An automatic time-stepping algorithm associated with the solver was implemented, which adjusts the time steps based on the thermal gradients. Specifically, finer time steps were used in regions with high thermal gradients, and coarser time steps in regions with low thermal gradients. The metal deposition was modelled through the implementation of the quiet element method [42] in which the thermal conductivity in the region where no deposition has occurred is reduced to a negligible level. As the heat source moves across a material element, the thermal conductivity is incrementally restored to its original value.

The numerically predicted thermal profiles were compared with the experimentally measured temperatures at two points on the substrate in a single bead-on-plate experiment with a travel speed of 5 mm s^{-1} and the results are shown in Fig. 3. The thermocouples were located in the middle of the substrate, 8 mm and 16 mm away from the centre line of the deposited bead. The results indicate a reasonable agreement between the numerically predicted and experimentally measured temperatures. The deviation between the peak temperature obtained from the numerical simulation and that measured in the experiments is less than 3%. This slight deviation can be attributed to the uncertainties in the temperature-dependent material properties and to simplifications made during the development of the model. However, as the purpose of the current study is to compare the relative variation in the cooling rates of the deposited beads between 800 °C and 500 °C, this deviation is considered acceptable.

Table 2 – The double ellipsoidal heat source parameters used in the thermal simulations.

Heat source parameter	Value
Front ellipsoidal length (a_f)	2.217 mm
Rear ellipsoidal length (a_r)	4.435 mm
Half-width of the melt pool (b)	2.217 mm
Depth of the melt pool (d)	1.885 mm
Front power distribution factor (f_f)	0.7
Rear power distribution factor (f_r)	1.3
Gaussian parameter (M)	3.0
Heat transfer efficiency (η)	0.85

2.3. *Microstructural characterization*

Transverse cross-sections were extracted from the middle of the deposits for microstructural characterization and microhardness measurements. The transverse cross-sections were mounted, ground and polished with colloidal diamond suspensions of 3 μm and 1 μm. Polished samples were etched with a 2% Nital solution and the microstructural features of the samples were investigated with optical microscopy (Olympus BX60 M and Keyence VHX-5000) and scanning electron microscopy, using a Jeol JSM-IT200 InTouch Scope with an accelerating voltage of 20 kV and probe current of 4 mA.

Phase analysis of the functionally graded sample was determined by means of X-ray diffraction (XRD) conducted using a Bruker D8-Advance diffractometer utilising a Co Kα radiation source and scanning the 2θ range from 30° to 150°. Each step in the scan had a counting time of 2 s and a step size of 0.04°. The XRD measurements were made with a beam size of 0.5 mm. The data obtained from the experiments were analyzed using Bruker's DiffracSuite EVA software (version 6.0), Profex/BGMN module. Rietveld refinement was employed to quantify the volume fractions of retained austenite (RA).

All Vickers hardness measurements were performed with a Dura-scan 70 (Struers) hardness tester with a dwell time of 15 s. Vickers hardness measurements on single bead deposits were achieved by averaging over eight indents at 0.1 kg load. Hardness measurements on functionally graded samples were performed along the build direction with a load of 1 kg. Another set of hardness measurements was made on the low heat input region with a load of 0.2 kg on ten points to explore the local hardness variations.

2.4. *Profilometry-based indentation plastometry*

Due to the sandwich structure's limited overall height of 23 mm and small size of each microstructural zone (~7 mm) it was challenging to create a macro-sized tensile specimen. Profilometry-based indentation plastometry (PIP) measurements were therefore performed on a transverse cross-section to estimate the yield and ultimate tensile strength. The process of estimating mechanical properties using PIP comprises: indenting the specimen, extracting the indentation profile and iteratively running finite-element models based on the indentation to estimate the parameters of the Voce relationship [43] to determine the true stress-strain relationship. Details of the PIP measurement are described elsewhere [44–48] and are not repeated here.

The metallographically prepared samples were placed on the load cell of the plastometer, and a spherical indenter with a diameter of 1 mm was used. An indent was made for PIP measurements in all three regions of the sample. The

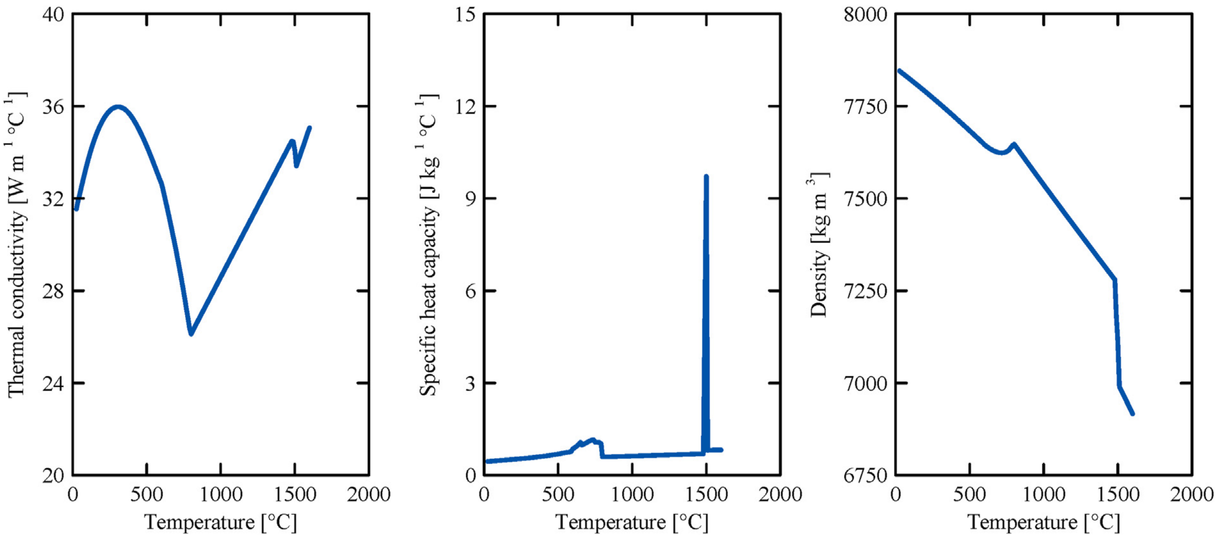

Fig. 2 – Temperature-dependent material properties of the high-strength steel (Lincoln Electric LNM MoNiVa) employed in the thermal simulations.

selection of indentation load is performed by ensuring that the ratio of indentation depth to the radius of the indenter, known as the penetration ratio, falls within the range of 10%–15%. A contacting stylus profilometer with a depth resolution of 1 μm was used to extract the profile of the indent made. A Young's modulus of 200 GPa and a Poisson's ratio of 0.3 were employed as the inputs to estimate the parameters of the Voce relationship.

3. Results and discussion

3.1. Single bead-on-plate experiments

The single bead-on-plate experiments with different travel speeds give an estimate of the range of cooling rates, microstructure and hardness observed by changes in process parameters. Additionally, analysing the bead geometry, including width, height, penetration depth and bead shape, provided insights into fusion between successive layers in a rectangular block. Single bead width was employed in the determination of the hatch spacing for improved layer bonding and reduced defects.

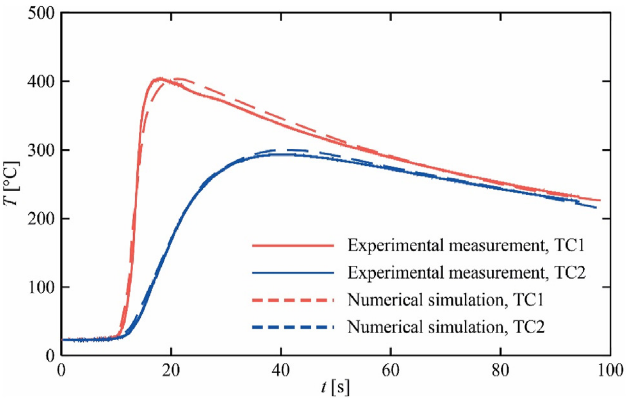

Fig. 3 – Comparison of the numerically predicted and experimentally measured temperatures at two monitoring points located in the middle of the substrate, 8 mm and 16 mm away from the centre line of the deposited bead. Data are collected from the single bead-on-plate experiments with a travel speed of 5 mm s^{-1}.

Single bead-on-plate depositions of 120 mm in length were executed using travel speeds ranging from 5 mm s^{-1} to 20 mm s^{-1} with intervals of 3 mm s^{-1}. The microstructural variations in single bead-on-plate depositions are associated with the cooling rates that the material experiences. Cooling rates within the temperature range of 800 °C–500 °C during bead-on-plate experiments were estimated through numerical simulations for various travel speeds, and the results are reported in Table 3. The cooling rate for a bead deposited with a travel speed of 8 mm s^{-1} differs by a factor greater than three from that for a bead deposited with a travel speed of 20 mm s^{-1}, resulting in different microstructures as indicated in the continuous cooling transformation (CCT) diagram shown in Fig. 4. A continuous cooling transformation (CCT) curve obtained from an artificial neural network (ANN)-based model (based on the composition mentioned in Table 1) is used indicating a critical cooling rate of 59 °C s^{-1} that results in a fully martensitic transformation [49]. Additionally, the material will predominantly transform into ferrite at low cooling rates. Based on the cooling rates for beads deposited at travel

Table 3 – Numerically predicted cooling rates for different travel speeds for single bead-on-plate experiments.

Travel speed (mm s^{-1})	Heat input (J mm^{-1})	Average cooling rate between 800 °C and 500 °C (°C s^{-1})
5	782	20
8	489	53
11	356	90
14	279	128
17	230	168
20	196	189

speeds of 8 mm s^{-1} and 20 mm s^{-1}, the CCT diagram suggests that beads deposited at the lower speed will exhibit a bainitic microstructure (comprising of upper bainite and acicular ferrite) while those deposited at the higher speed will exhibit a fully martensitic microstructure. It should be noted that the bead deposited at a travel speed of 5 mm s^{-1} had the highest heat input, and trial multiple bead depositions resulted in excessive thermal energy accumulation. Hence, a travel speed of 8 mm s^{-1} was employed to deposit material in the high heat input (HHI) region of the functionally graded part shown in Fig. 1.

Optical micrographs obtained from the single beads deposited at speeds of 8 mm s^{-1} and 20 mm s^{-1} are shown in Fig. 5. The bead deposited at low speed shows a mixed microstructure of polygonal ferrite, acicular ferrite, bainite and low carbon martensite, resembling the microstructure observed in beads deposited at a speed of 5 mm s^{-1}. Such a mixed microstructure is typical in high-strength steel welds [50,51]. Optical micrographs of samples deposited at higher travel speeds, such as 17 mm s^{-1} and 20 mm s^{-1}, indicate a fully martensitic microstructure with the presence of a small amount of grain boundary ferrite or Widmanstätten ferrite, consistent with the CCT diagram depicted in Fig. 4. Fig. 6 shows the average hardness confirming the expected trend of increasing hardness with increasing travel speed. The sample deposited at 5 mm s^{-1} has a hardness of approximately 260 HV0.1. The highest hardness of 440 HV0.1 was observed for the sample deposited at 20 mm s^{-1}, which can be attributed to the rapid cooling experienced by the deposited material and higher martensitic phase fractions. This variation in hardness with changes in travel speed demonstrates the potential of wire arc additive manufacturing to achieve graded microstructures and properties by controlling process parameters in high-strength steels.

3.2. *Functionally graded block*

The process parameters for the building of the functionally graded block were chosen based on the results of the single bead-on-plate experiments, as outlined in Table 4. Deposition of the low heat input region was devoid of humping defects even though a relatively high travel speed was employed. The number and placement of successive weld passes are described in section 2.1.

3.2.1. *Macrostructure and grain structure*

Fig. 7 shows a transverse cross-section of the functionally graded block, revealing the absence of porosity and lack of fusion. Fig. 7(b) is a high-magnification optical micrograph of the interface between the HHI region (bottom) and the LHI region (top). A marked change in microstructural features at the interface between the two regions is visible. The HHI region exhibits higher fractions of coarse grains, while finer grains are observed in the LHI region. When molten material is deposited on a substrate or base material with the same crystal structure, epitaxial growth is preferred over nucleation in the melt pool [28]. During epitaxial growth, nucleating grains inherit the orientation from the unmelted grains at the fusion boundary. The preference for epitaxial growth is due to the negligible activation barrier. The direction of the

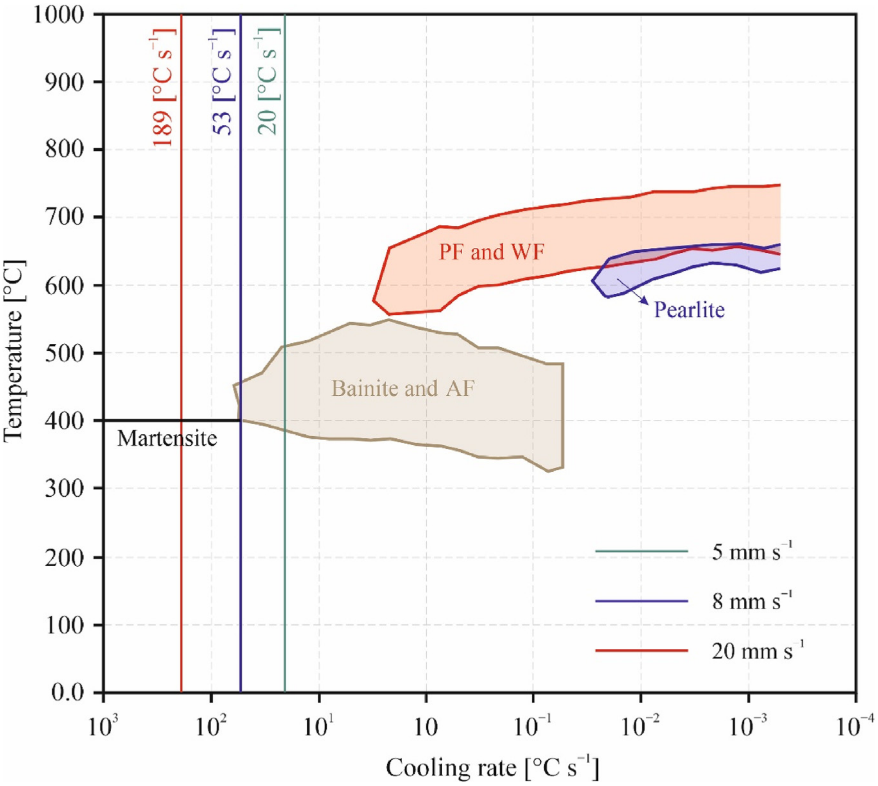

Fig. 4 – The CCT (continuous cooling transformation) diagram corresponding to the high-strength steel composition employed in the present study (see Table 1). The data is taken from Ref. [49].

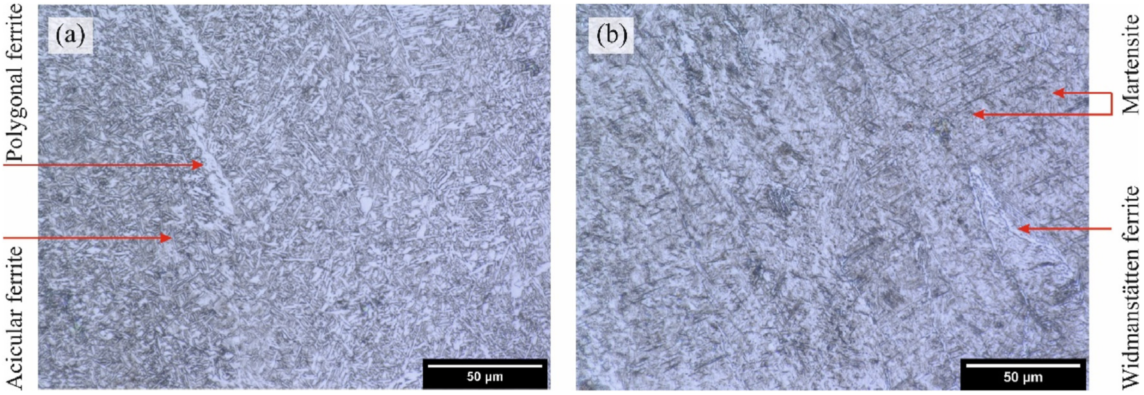

Fig. 5 – Optical micrographs of the beads deposited at different travel speeds: (a) 8 mm s^{-1} and (b) 20 mm s^{-1}.

maximum temperature gradient during the process determines the orientation of the columnar grain growth. In materials with cubic crystal structures such as steels, the favourable growth direction is <100> [28]. Grains with a preferential growth direction that is favourably oriented to the maximum temperature gradient direction grow faster and crowd out the grains oriented less favourably, resulting in a competitive growth mechanism, as shown in Fig. 8. Along the central region of the sample, due to bidirectional scanning and increasing build height, the maximum temperature gradient direction aligns along the build direction. Epitaxial columnar grains are dependent on the solid-liquid interface curvature initially but towards the centre of a bead, they are observed to be oriented along the build direction. Near the edge of the sample, it can be seen that the columnar grains are oriented towards the sidewalls rather than along the build direction. This is due to edge beads being deposited on curved surfaces resulting in a change of boundary conditions and the rotation of the maximum temperature gradient direction [52].

The morphology of the microstructure formed during the solidification can exhibit columnar or equiaxed structures or a combination of both forms. The solidification velocity (R) and magnitude of temperature gradient (G) are primary factors that influence the evolution of grain morphology. Relatively high values of G/R tend to result in the formation of a columnar grains extending over several layers, which is a common characteristic in the microstructures of additively manufactured components [53,54]. However, the solidification microstructure of the functionally graded block did not exhibit large directionally solidified columnar grains extending over multiple layers due to the bidirectional scanning strategy employed in the experiments, which leads to a change in the maximum thermal gradient direction [55]. Nevertheless, columnar grains can be still observed within a bead.

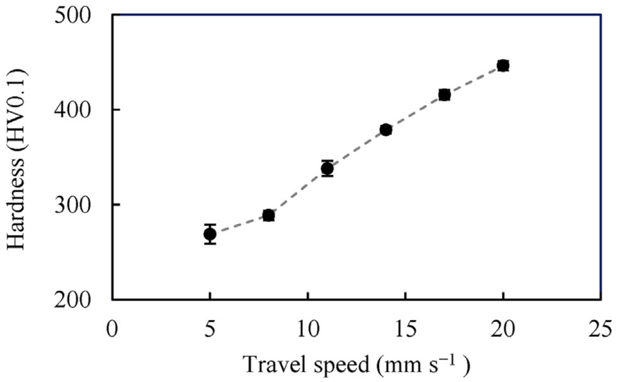

Fig. 6 – The variation of the Vickers hardness with travel speed for single bead-on-plate deposits.

An equiaxed-grained region is identified in the vicinity of the fusion zone of each bead, which is associated with the formation of heat-affected zones (HAZ) [56]. Deposition of a subsequent bead results in the partial remelting of the previous bead. The regions located immediately below the partially remelted zone are subjected to high temperatures in the range of 1350 °C for a short period of time leading to grain coarsening and the formation of coarse, equiaxed austenite grains. The regions that remained below the Ac_3 critical temperature retain their columnar structure, as depicted in Fig. 8; as a result, a periodic occurrence of equiaxed and columnar grains within the block can be observed.

3.2.2. *Microstructure evolution in the high heat input zone*

Optical and SEM micrographs from both HHI regions are shown in Fig. 9. The micrographs indicate the presence of similar microstructural constituents in both HHI regions. Microstructural constituents of the high heat input regions are primarily polygonal ferrite, acicular ferrite upper bainite, granular bainite and traces of martensite. This microstructure is indicative of lower strength and hardness but higher ductility and toughness compared to a fully martensitic microstructure. The HHI bottom region experiences higher cooling rates initially due to the higher heat diffusion to the substrate, resulting in a somewhat higher martensitic content in the HHI bottom region than HHI top region. However, HHI bottom region undergoes severe tempering due to the deposition of the subsequent beads in the LHI region and the HHI top region and because of this, tempered martensite can be observed in the HHI bottom region.

Based on the CCT diagram presented in Fig. 4, bainite and acicular ferrite form at intermediate cooling rates. The formation of upper bainite and granular bainite occurs due to the diffusion-less transformation of austenite to fine plates of ferrite supersaturated with carbon. Carbon during bainite

Table 4 – The set of process parameters employed to manufacture a functionally graded rectangular block.

Region	Wire feed rate	Travel speed	Average Voltage	Average Current	Heat input
HHI	6 m min^{-1}	8 mm s^{-1}	23 V	179 A	489 J mm^{-1}
LHI	6 m min^{-1}	20 mm s^{-1}	23 V	177 A	196 J mm^{-1}

formation is partitioned to austenite between the individual plates, enriching the austenite and resulting in the precipitation of cementite. Parallel sheaths or subunits of bainite have low-angle grain boundaries, enabling crack propagation during cleavage fracture. Coarse granular and upper bainite microstructures lead to inferior mechanical properties and play an important role in the reduction of fracture toughness of the deposited part [25].

Acicular ferrite also forms at approximately the same temperature as bainite. Acicular ferrite nucleates on nonmetallic inclusions within prior austenite grains (PAG) and has random crystallographic orientations, with high misorientation angles (larger than 50°). The fine-grain size and random orientation of acicular ferrite grains impart better strength and enable crack deflection in the event of cleavage crack propagation. In additive manufacturing of high-strength steels for structural applications, acicular ferrite is considered to be a desirable microstructural feature [25,57].

The XRD patterns obtained from HHI regions are given in Fig. 10. The predominant presence of ferrite is confirmed by the peaks of {110},{200} and {211}. Austenite peaks of {111},{200} and {220} confirm the presence of Retained Austenite (RA). The retained austenite fractions in both HHI regions are quantitatively determined as given in Table 5 and are consistent with previous studies on continuous cooling of high strength low alloyed steels [58–60]. When austenitized material is continuously cooled at moderate cooling rates (5 °C s^{-1} to 30 °C s^{-1}), the decomposition of austenite commences with the formation of grain boundary ferrite along the prior austenite grain boundaries. The formation of grain boundary ferrite leads to the rejection of carbon to the adjacent austenite increasing the carbon content. Partitioning of carbon to austenite continues during subsequent decomposition to bainite and acicular ferrite. The martensite transformation start temperature depends inversely on the carbon content of the parent austenite grains due to the increased stability of carbon-enriched austenite [50]. In the present case, the carbon concentration in the retained austenite (C_γ) is estimated from the lattice parameter using equation (2) [61].

$$\alpha_\gamma = 3.573 + 0.033C_\gamma + 0.00095Mn - 0.0002Ni + 0.0006Cr + 0.0031Mo + 0.0018V \tag{2}$$

where α_γ is the lattice constant of austenite in (Å) and the material composition of manganese (Mn), nickel (Ni), chromium (Cr), molybdenum (Mo) and vanadium (V) are in weight percent. The lattice parameter of austenite is 3.605 Å and was obtained from XRD measurements performed on the HHI top region.

From equation (2), the carbon concentration (C_γ) is estimated to be 0.97%, which is subsequently employed to estimate the M_s temperature of carbon-enriched austenite using equation (3) [61].

$$M_s = 539 - 423C - 30.4Mn - 17.7Ni - 12.1Cr - 11Si - 7Mo \tag{3}$$

where the material composition is given in weight percent. The calculated M_s is 76.3 °C whereas the calculated M_s for the nominal composition of the steel used in the present study is

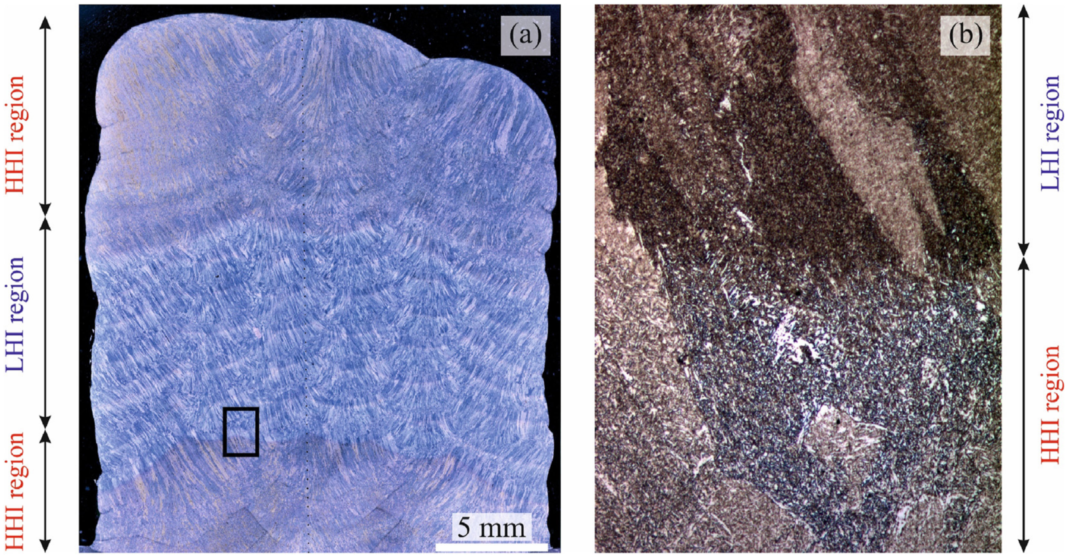

Fig. 7 – (a) Transverse cross-section of the functionally graded block and (b) the interface between low heat input (LHI) and high heat input (HHI) regions (b). Subfigure (b) depicts an enlargement of the area designated by the black rectangle in subfigure (a).

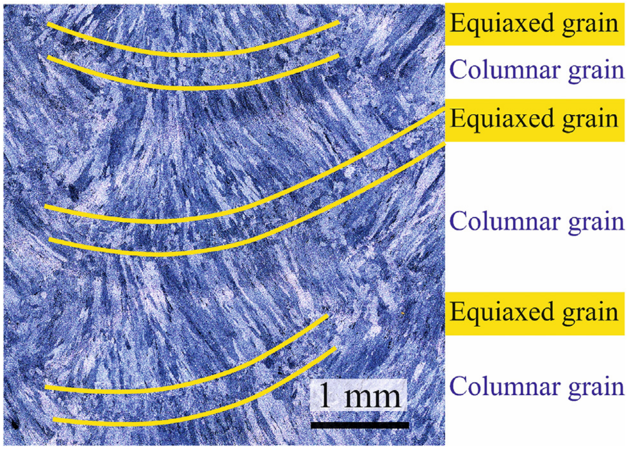

Fig. 8 – Columnar and equiaxed grains observed in the transverse cross-section of the low heat input (LHI) region of the sample. The areas situated between the yellow lines show equiaxed grains.

420 °C. Higher carbon content stabilizes the austenite and delays its transformation to a BCC or BCT structure. The low martensite transformation temperature results in an incomplete transformation of remaining austenite to martensite, leading to the formation of martensite-austenite (MA) islands. The formation of MA islands is escalated in the inter-critically reheated regions due to enhanced enrichment of partially transformed austenite [62,63].

A higher magnification image of the HHI region is provided in Fig. 11. Martensite austenite islands are observed between bainite laths and along prior austenite grain boundaries. MA islands generally have a stringer or blocky morphology [64], which is also confirmed in Fig. 11. The presence of MA islands with stringer morphology is detrimental to the low-temperature toughness as it is easily debonded from the surrounding matrix. It is also reported that the presence of MA islands with stringer morphology at prior austenite grain boundaries increases local stress concentration, and consequently the formation of microcracks and initiation of cleavage fracture. Likewise, debonding of MA particles may occur in the case of isolated blocky MA islands, but these are less likely to initiate fracture [65].

To improve the impact toughness of WAAM-deposited high-strength steels, a reduction in the volume fraction of MA islands is vital. Reducing the size and increasing the degree of dispersion would avoid the detrimental effects of MA constituents. Post-WAAM heat treatments or the use of lower heat inputs during welding can be employed to achieve lower fractions of MA constituents [66]. Conventional heat treatments like tempering for 30 min do not significantly increase the impact toughness of the material even though the MA islands are decomposed. Lack of improvement of impact properties on tempering can be linked to the formation of carbides at grain boundaries [67]. Hence complex heat treatments leading to inter-critical heat treatment and tempering have been utilized in previous studies for the decomposition of MA islands and the formation of fine retained austenite which improves the impact toughness [67].

3.2.3. *Microstructure evolution in the low heat input zone*

The microstructure in the low heat input region comprises low carbon martensite, grain boundary ferrite and Widmanstätten ferrite as shown in Fig. 12. An interpass

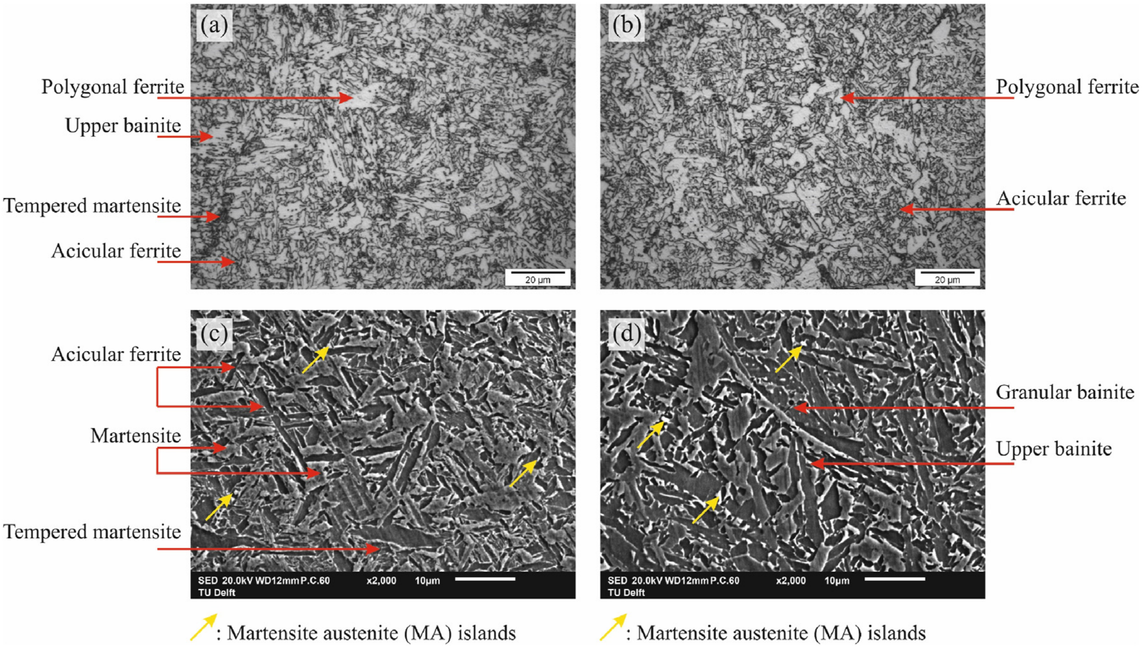

Fig. 9 – Optical micrographs showing (a) HHI Bottom region and (b) HHI top region and SEM micrographs showing (c) HHI bottom region and (d) HHI top region. A mixed microstructure of different ferrite morphologies and martensite is observed. The yellow arrows indicate martensite austenite (MA) islands.

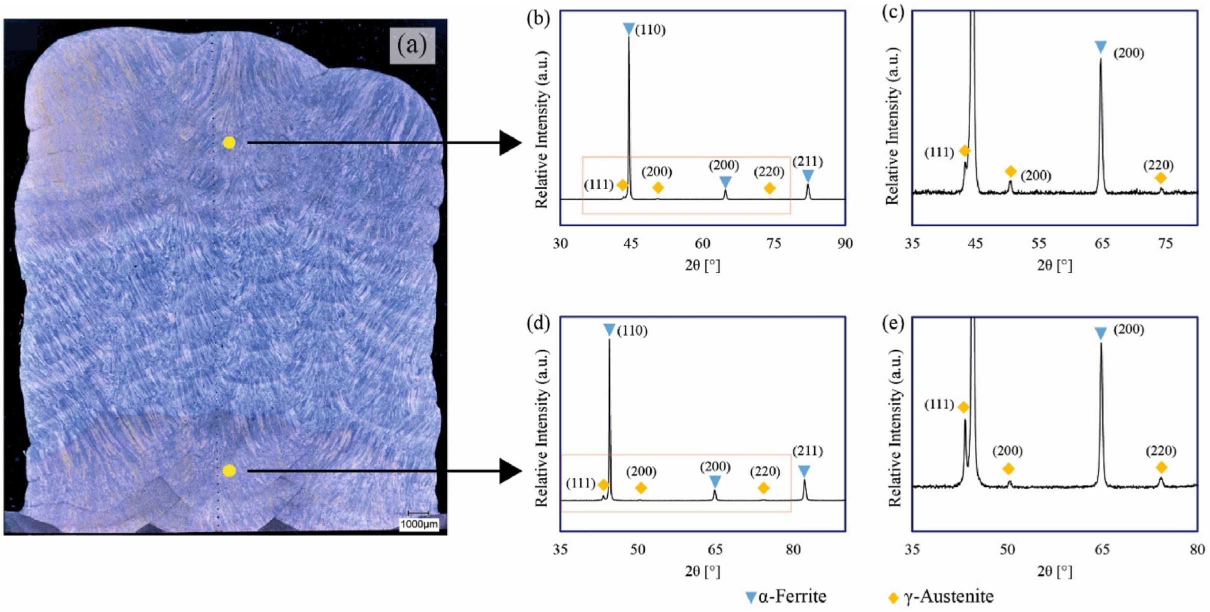

Fig. 10 – (a) Macrograph of the functionally graded block showing the positions where X-Ray Diffraction (XRD) patterns are recorded. (b) and (d) The XRD patterns obtained from the top high heat input (HHI) region and bottom HHI region, respectively. (c) and (e) Magnified images of the retained austenite peaks in the XRD patterns of both HHI regions.

temperature of 50 °C was maintained in the low heat input region, stimulating increased heat extraction by the deposited beads. Higher heat extraction from beads results in higher cooling rates compared to beads in the HHI region, which will favour the formation of non-equilibrium phases such as martensite.

Martensite is formed in steels at high cooling rates by the displacive phase transformation of austenite. Martensite is a supersaturated solution of carbon in ferritic iron with a body-centered tetragonal structure (BCT). Higher dislocation densities in the substructure along with the shape of crystals impart higher strength and hardness and reduced ductility of martensite when compared to other ferrite morphologies [25,68].

A SEM micrograph from the low heat input region (Fig. 13) indicates precipitation of cementite, indicating a tempered martensitic microstructure. Tempering in the low heat input region can be attributed to thermal treatment between 250 °C and the Ac_1 temperature experienced by the material due to the deposition of subsequent HHI and LHI beads. During tempering, excess carbon in martensite and bainite is precipitated as cementite particles at the lath boundaries, and tempering is more predominant in martensite. Low carbon content in steels increases the martensitic transformation temperatures, M_s and M_f. It is observed that in low-carbon steels, the transformed martensite undergoes tempering during the remainder of the cooling process, also known as auto-tempering. The martensite start temperature for the steel used in the present study is estimated to be 420 °C given by equation (3). Tempering of martensite instigates enhancement of mechanical properties like toughness, but a reduction in strength and hardness. Reduction of strength and hardness during tempering is also linked to dislocation recovery, leading to a reduction of dislocation densities [69]. Peak temperatures of 600 °C or more during tempering can cause a considerable reduction in hardness [25].

Table 5 – The fraction of the retained austenite phase estimated from X-Ray Diffraction (XRD) measurements.

Region	Retained austenite phase fraction
HHI-top	5% ± 1%
HHI-bottom	4% ± 1%

Martensite austenite islands were rarely observed within the LHI regions and those that had a smaller size than the MA islands in the HHI regions, which is confirmed by the XRD measurements presented in Fig. 14 showing that no retained austenite peaks were detected. Similar to the HHI regions, ferrite peaks of {110}, {200} and {211} were observed. Due to the increased cooling rates experienced in the LHI region, limited diffusion of carbon happens during austenite decomposition. After the formation of the grain boundary ferrite/Widmanstätten ferrite, the remaining austenite is transformed into martensite. Only XRD peaks corresponding to only the BCC crystal structures were observed. Although martensite has a body-centered tetragonal crystal structure, the tetragonality of the martensite is low due to the low carbon content of the steel, which renders it difficult to distinguish by XRD. Additionally, cementite precipitation during tempering was not detected by XRD due to the small size and low concentration of cementite.

3.2.4. *Vickers hardness and microstructure correlation*

The hardness profile of the sample along the build direction is given in Fig. 15. The hardness of the high heat input

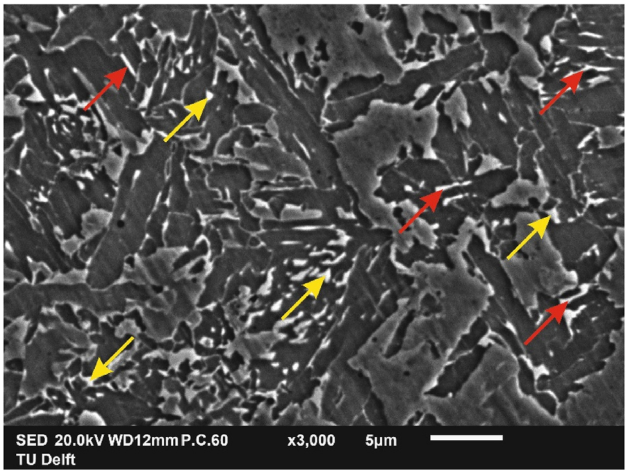

Fig. 11 – A higher magnification image of the high heat input (HHI) region displays diverse morphologies of MA islands. The red arrows indicate stringer morphologies and the yellow arrows indicate blocky morphologies.

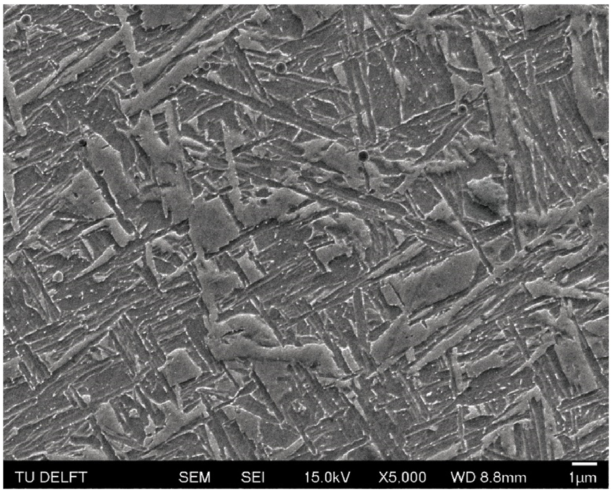

Fig. 13 – A magnified view of the low heat input (LHI) region exhibiting carbides in the tempered martensite within the LHI regions.

regions is almost homogenous around 250 HV1. The lower hardness in the HHI regions can be attributed to the occurrence of a higher ferrite fraction in the microstructure. The low standard deviation in hardness values in HHI regions is indicative of a relatively homogenous microstructure. For the low heat input region, the hardness values are elevated to a maximum of 360 HV1 indicating successful grading of properties. The comparatively higher micro-hardness in the low heat input region can result from the formation of higher martensite phase fractions; however, hardness values in the low heat input region show a high scatter, fluctuating roughly between 312 HV1 and 360 HV1. It should be noted that the standard deviation in hardness values corresponding to the LHI region is approximately four times higher than that of HHI regions, indicating an inhomogeneous microstructure and properties.

The lower hardness values observed in the low heat input region are attributed to the presence of a white-banded region which could easily be mistaken for the fusion line. The white band region and fusion line are indicated in Fig. 16(b). The distance between the white region and the fusion line is fairly constant and is measured to be 539 μm ± 14 μm. Softened regions with lower hardness have already been reported for multi-pass welding of low-carbon steels and ultra-high-strength steels [70,71]. To comprehend the influence of the microstructure in the white band on hardness, hardness measurements were performed with a load of 0.2 kg across a white region (Fig. 16). The hardness drops from 350 HV to 280 HV when the indent location is in the white region (Fig. 16(a)). A comparison of the scanning electron micrographs obtained from the beads in the LHI region (see Fig. 12(b)) and the white band region (see Fig. 17) reveals that the microstructural constituents in both regions are significantly different. Martensite (tempered and untempered) is present within the beads, while the white regions have a mixed microstructure of polygonal ferrite, bainite and martensite (tempered and untempered); this variation is also implied in the hardness profile shown in Fig. 15.

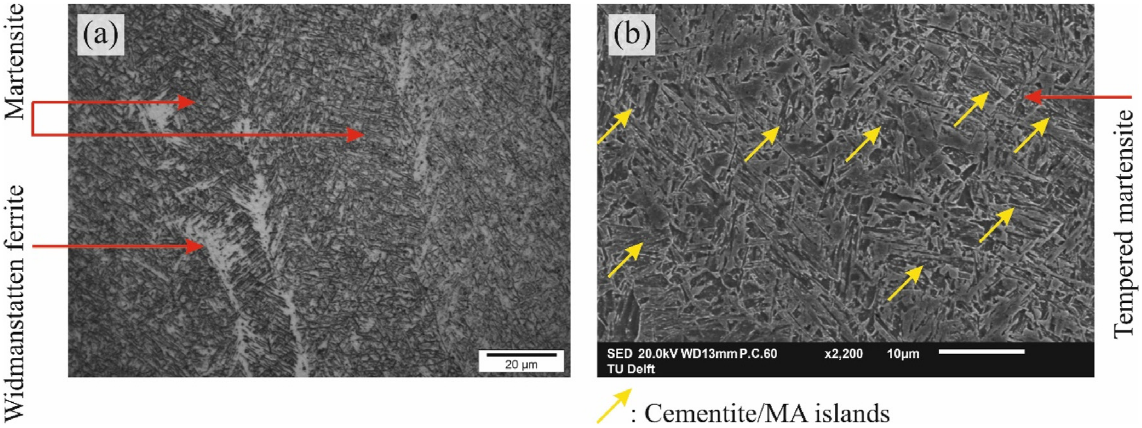

Fig. 12 – (a) Optical and (b) SEM micrograph from the low heat input (LHI) region. The yellow arrows indicate the presence of cementite particles or MA islands.

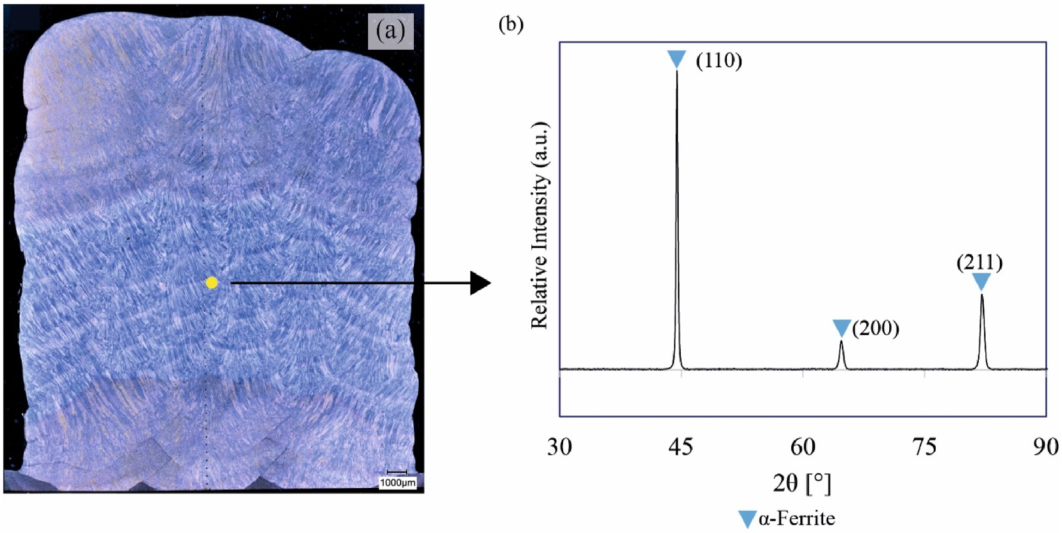

Fig. 14 – (a) Macrograph of the functionally graded block showing the location where the X-Ray Diffraction (XRD) measurement was conducted. (b) The XRD pattern was obtained from the low heat input (LHI) region, displaying only ferrite peaks.

The softening observed in the white regions could be due to the recrystallization of lath martensite grains [72], tempering or the formation of relatively softer phases like bainite, acicular ferrite or polygonal ferrite during cooling. Recrystallization of lath martensite in steels occurs in the temperature region between 350 °C and 700 °C causing coarsening of martensite laths, formation of dislocation-free equiaxed grains and precipitation of carbides [25,69]. However, it can be observed in Fig. 17 that the ferrite grains have mostly an elongated morphology and cannot be linked entirely to the recrystallization phenomenon [25]. Previous research on white regions formed during multi-pass welding of HSLA-100 steels articulated the presence of tempered martensite in white regions leading to lower hardness [70]. The white regions can correspond to the softening associated with the inter-critically heat-affected zone (peak temperature is between Ac_1 and Ac_3) and the subcritical heat-affected zone (peak temperature $\leq Ac_1$) [71,73].

When the material is heated to the inter-critical region, austenite nucleates along the prior austenite grain boundaries and martensitic laths. The remaining untransformed martensite undergoes severe tempering. On subsequent cooling, the austenite formed at inter-critical temperatures is transformed into different ferritic morphologies or martensite depending on the cooling rate [74]. Cooling rates experienced by the material in the inter-critical heat-affected zone (ICHAZ) regions are less than the critical cooling rate for complete martensite transformation, which is evident from the observed microstructure in Fig. 17. In the subcritical heat-affected zone with a peak temperature approximately equal

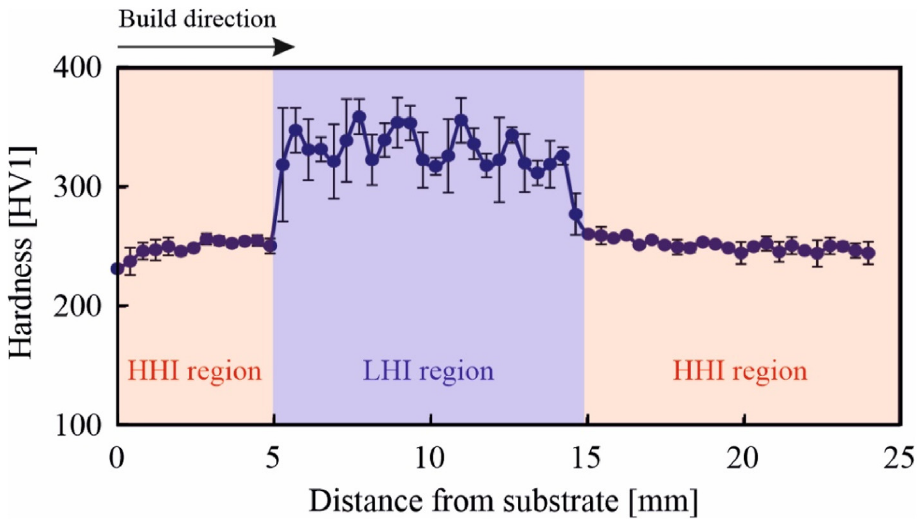

Fig. 15 – Hardness measurements taken along the build direction on the transverse cross-section of the functionally graded block.

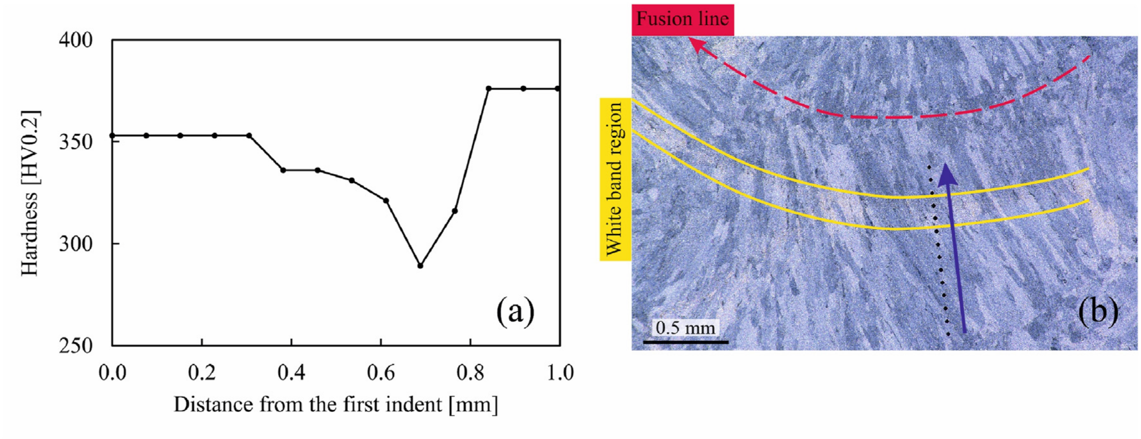

Fig. 16 – (a) Hardness measurements performed across a white band, verifying the occurrence of softening. (b) Indentations made across the white band region. The area between the yellow lines represents the white band region. The red dashed line indicates the fusion line.

to Ac_1, no austenite transformation occurs and martensite undergoes tempering resulting in the formation of soft-tempered martensite [71].

The occurrence of white bands in the high heat input regions is also a possibility. Cooling rates experienced by the material within the bead or the white band regions in the HHI zone are not sufficiently different to cause a drastic variation in microstructure and hardness. Nonetheless, the presence of similar microstructural constituents in both the bead and white band renders it difficult to distinguish the white bands in the high heat input region based on microstructural observations or from hardness measurements. The high-heat-input regions have a more homogenous microstructure and hardness than the low-heat-input regions.

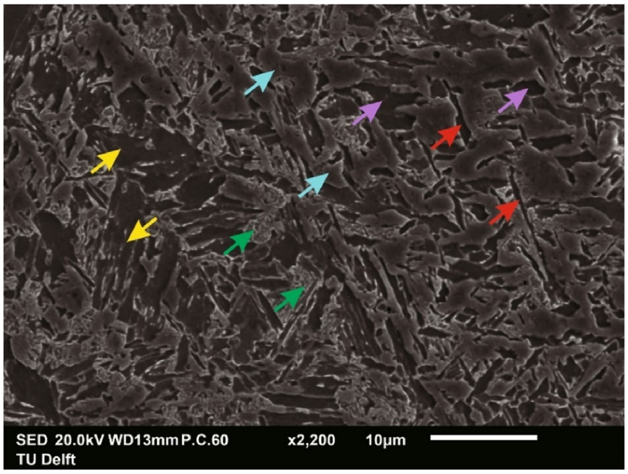

Fig. 17 – Microstructure in the white band regions indicating a mixed microstructure of different ferrite morphologies and martensite. Coloured arrows denote different microstructural constituents. Yellow: Upper bainite, Red: Acicular ferrite, Green: Lower bainite or tempered martensite, Purple: Polygonal ferrite and Blue: Untempered martensite.

Since hardness measurements are indicative of the strength of the material it can also be inferred that yield strength and ultimate tensile strength of the material are higher in the LHI regions. Generally, the uniaxial flow strength of a material is assumed to be approximately three times the hardness [75].

3.2.5. *Profilometry-based indentation plastometry (PIP)*

Stress-strain curves estimated from the PIP measurements corresponding to indents from each region are given in Fig. 18. Both the bottom and top HHI regions indicate lower yield (50%) and ultimate tensile strength (34%) than the LHI region. Stress-strain curves from both the HHI regions indicated similar behaviour and the values of yield strength (YS) and ultimate tensile strength (UTS) are comparable. The calculated strength properties for each indent are given in Table 6.

The ultimate tensile strength of HHI regions is comparable with the strength properties corresponding to previous research from Rodrigues *et al.* [7] and Rodideal *et al.* [18], which used similar heat inputs. In contrast to previous studies, the LHI region possesses higher tensile strength. This is due to the lower interpass temperature maintained in the LHI region in addition to the lower heat input. Material properties of the as-welded material obtained from the supplier data sheet indicate that the LHI region has almost 38% increase in yield stress and 25% increase in UTS. Conversely, the HHI regions had an 11% lower yield stress and 7% lower UTS than indicated in the datasheet.

For the PIP measurement in the LHI region, the indent was made to avoid an overlap over the white band regions to minimise the effect of softening caused by the white band regions. The LHI region has a lower uniform elongation of 2.3% because of the lower ductility associated with the martensite phase. The uniform elongation in both HHI regions is higher at approximately 10%. Subjecting such a sandwich structure to uniaxial loading along the build direction can therefore lead to non-uniform strain distribution and failure in the HHI regions.

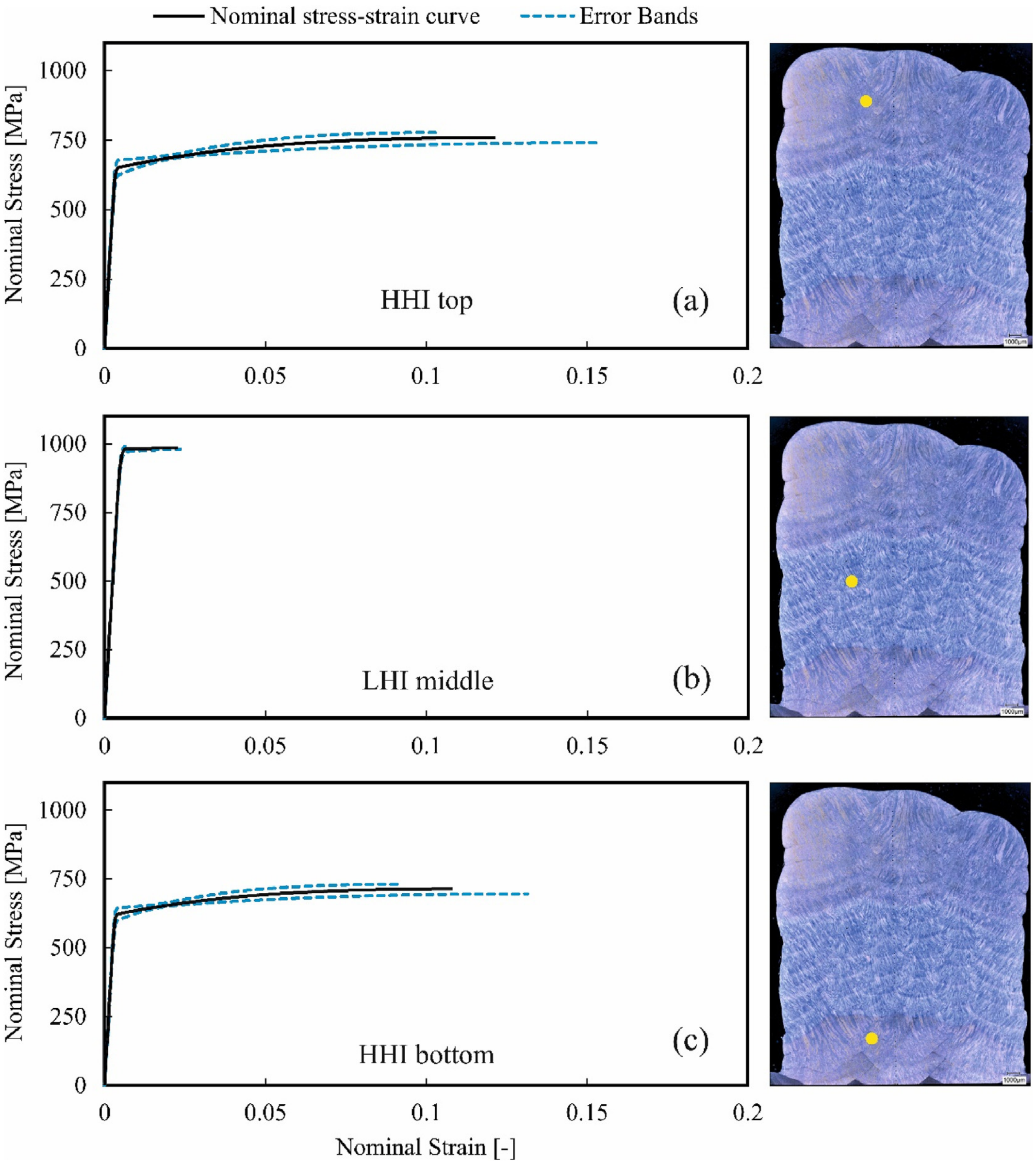

Fig. 18 – Nominal stress-strain curves derived from profilometry-based indentation plastometry (PIP) measurements on (a) the top high heat input (HHI) region, (b) the middle low heat input (LHI) region, and (c) the bottom HHI region. The yellow dots indicate the location of indents for PIP measurements.

Table 6 – The yield strength, ultimate tensile strength (UTS), and uniform elongation obtained from profilometry-based indentation plastometry (PIP) measurements.

Test Location	Yield Strength (MPa)	UTS (MPa)	Uniform elongation (%)
HHI Bottom	619 ± 25	713 (695–730)	10.8 (9.2–13.2)
LHI Middle	981 ± 13	984 (980–992)	2.3 (0.6–2.4)
HHI Top	648 ± 29	758 (740–777)	12.2 (10.5–15.4)
ER110S-G wire (from the material certificate)	710	790	

4. Conclusions

The control of microstructure and mechanical properties of high-strength steel S690 through electric arc-based wire arc additive manufacturing was explored in the present work. In contrast to previous studies that relied on compositional variations or in-situ thermo-mechanical methods to control the properties, process parameters were adjusted to regulate the energy input and produce spatially varied microstructures. Based on the results of the present study, the following conclusions are drawn.

- Employing higher travel speeds in single bead-on-plate experiments resulted in increased cooling rates between 800 °C and 500 °C, higher martensitic phase fractions, and higher hardness. This demonstrates the possibility of functional grading by adjusting travel speed in electric arc-based additive manufacturing.

- The hardness measurements made on the transverse cross-sections of the rectangular block in the build direction confirmed microstructural grading, with low heat-input regions displaying higher and fluctuating hardness values, and high heat-input regions displaying lower and more uniform hardness.
- The adjustment of process parameters allowed for the observation of spatial variation in microstructural constituents in the rectangular block, indicating successful microstructural grading. The use of lower heat input during the deposition of high-strength steels combined with an inter-bead temperature of 50 °C led to higher cooling rates, resulting in the formation of martensite. Conversely, increasing the heat input and inter-pass temperature reduced the cooling rate, producing a mixed microstructure of polygonal and acicular ferrite, bainite, and martensite that could be correlated to the hardness measurements.
- Fluctuations in the hardness profiles corresponding to low heat-input regions were caused by the occurrence of inter-critically reheated heat-affected zones, which possessed lower hardness due to the mixed microstructure of martensite (tempered and untempered), bainite, and ferrite. The use of lower travel speeds to increase cooling rates can create microstructural inhomogeneity, leading to localized soft zones with considerably lower hardness than the surrounding material.
- Profilometry-based plastometry measurements indicated an increase in the yield and tensile strength (by approximately 150 MPa) and lower elongation (2.3%) for the low heat-input regions compared with the high-heat-input regions. Conversely, high heat-input regions displayed higher elongations (10.2% and 12.4%) due to the presence of grain boundary ferrite, acicular ferrite, and tempered martensite, indicating that these regions could accommodate larger deformations.

It should be noted that this study was limited to one high-strength low-alloy steel, but the methodology proposed for obtaining spatially varied microstructure and properties could be applied to other metallic materials. When combined with numerical simulations, this approach could lead to the fabrication of parts with control over the local mechanical properties. Future research should examine the effect of additional parameter combinations, improving manufacturing efficiency and performance evaluation of such tailor-made microstructures to exploit the potential of functional grading. Awareness of achievable properties in the design stage of parts should also be improved to achieve the full potential of functional grading of WAAM. Additionally, attention should be given to the certification process of functionally graded WAAM parts.

Data availability

The data that support the findings of this study are available from the corresponding author, A.B., upon reasonable request.

Declaration of competing interest

The authors declare that they have no known competing financial interests or personal relationships that could have appeared to influence the work reported in this paper.

Acknowledgement

This research was carried out under project number P16-46 pr3/S17024j, which is part of the AiM2XL program framework of the Partnership Program of the Materials innovation institute M2i (www.m2i.nl) and the Netherlands Organization for Scientific Research (www.nwo.nl). The research was conducted in collaboration with industrial partners and supported by the Rotterdam Field Lab Additive Manufacturing BV (RAMLAB) (www.ramlab.com).

The authors extend their gratitude to Mr Ruud Hendrikx, from the Department of Materials Science and Engineering at the Delft University of Technology, for his invaluable contribution to the X-ray analysis. They also express their appreciation to Mr Remko Seijffers, also from the same department, for his supportive role during the wire-arc additive manufacturing (WAAM) experiments. The authors are further thankful to Rebecca Reiff-Musgrove of Plastometrex for her support with the profilometry-based indentation plastometry (PIP) measurements.

REFERENCES

[1] Svetlizky D, Das M, Zheng B, Vyatskikh AL, Bose S, Bandyopadhyay A, et al. Directed energy deposition (DED) additive manufacturing: physical characteristics, defects, challenges and applications. Mater Today 2021;49:271–95. https://doi.org/10.1016/j.mattod.2021.03.020.

[2] Sames WJ, List FA, Pannala S, Dehoff RR, Babu SS. The metallurgy and processing science of metal additive manufacturing. Int Mater Rev 2016;61:315–60. https://doi.org/10.1080/09506608.2015.1116649.

[3] Wu B, Pan Z, Ding D, Cuiuri D, Li H, Xu J, et al. A review of the wire arc additive manufacturing of metals: properties, defects and quality improvement. J Manuf Process 2018;35:127–39. https://doi.org/10.1016/j.jmapro.2018.08.001.

[4] Williams SW, Martina F, Addison AC, Ding J, Pardal G, Colegrove P. Wire + arc additive manufacturing. Mater Sci Technol 2016;32. https://doi.org/10.1179/1743284715Y.0000000073.

[5] Kok Y, Tan XP, Wang P, Nai MLS, Loh NH, Liu E, et al. Anisotropy and heterogeneity of microstructure and mechanical properties in metal additive manufacturing: a critical review. Mater Des 2018;139:565–86. https://doi.org/10.1016/j.matdes.2017.11.021.

[6] Shamsaei N, Yadollahi A, Bian L, Thompson SM. An overview of Direct Laser Deposition for additive manufacturing; Part II: mechanical behavior, process parameter optimization and control. Addit Manuf 2015;8:12–35. https://doi.org/10.1016/j.addma.2015.07.002.

[7] Rodrigues TA, Duarte V, Avila JA, Santos TG, Miranda RM, Oliveira JP. Wire and arc additive manufacturing of HSLA steel: effect of thermal cycles on microstructure and

mechanical properties. Addit Manuf 2019;27:440–50. https://doi.org/10.1016/j.addma.2019.03.029.
[8] Le VT, Mai DS, Hoang QH. A study on wire and arc additive manufacturing of low-carbon steel components: process stability, microstructural and mechanical properties. J Brazilian Soc Mech Sci Eng 2020;42:480. https://doi.org/10.1007/s40430-020-02567-0.
[9] Ebrahimi A, Babu A, Kleijn CR, Hermans MJM, Richardson IM. The effect of groove shape on molten metal flow behaviour in gas metal arc welding. Materials 2021;14:7444. https://doi.org/10.3390/ma14237444.
[10] Ebrahimi A, Kleijn CR, Hermans MJM, Richardson IM. The effects of process parameters on melt-pool oscillatory behaviour in gas tungsten arc welding. J Phys D Appl Phys 2021;54:275303. https://doi.org/10.1088/1361-6463/abf808.
[11] Halisch C, Radel T, Tyralla D, Seefeld T. Measuring the melt pool size in a wire arc additive manufacturing process using a high dynamic range two-colored pyrometric camera. Weld World 2020;64:1349–56. https://doi.org/10.1007/s40194-020-00892-5.
[12] Xia C, Pan Z, Polden J, Li H, Xu Y, Chen S, et al. A review on wire arc additive manufacturing: monitoring, control and a framework of automated system. J Manuf Syst 2020;57:31–45. https://doi.org/10.1016/j.jmsy.2020.08.008.
[13] Ebrahimi A, Kleijn CR, Richardson IM. A simulation-based approach to characterise melt-pool oscillations during gas tungsten arc welding. Int J Heat Mass Tran 2021;164:120535. https://doi.org/10.1016/j.ijheatmasstransfer.2020.120535.
[14] Sun L, Jiang F, Huang R, Yuan D, Guo C, Wang J. Microstructure and mechanical properties of low-carbon high-strength steel fabricated by wire and arc additive manufacturing. Metals 2020;10. https://doi.org/10.3390/met10020216.
[15] Rafieazad M, Ghaffari M, Vahedi Nemani A, Nasiri A. Microstructural evolution and mechanical properties of a low-carbon low-alloy steel produced by wire arc additive manufacturing. Int J Adv Manuf Technol 2019;105:2121–34. https://doi.org/10.1007/s00170-019-04393-8.
[16] Rafieazad M, Nemani AV, Ghaffari M, Nasiri A. On microstructure and mechanical properties of a low-carbon low-alloy steel block fabricated by wire arc additive manufacturing. J Mater Eng Perform 2021;30:4937–45. https://doi.org/10.1007/s11665-021-05568-9.
[17] Duarte VR, Rodrigues TA, Schell N, Santos TG, Oliveira JP, Miranda RM. Wire and arc additive manufacturing of high-strength low-alloy steel: microstructure and mechanical properties. Adv Eng Mater 2021;23:2001036. https://doi.org/10.1002/adem.202001036.
[18] Rodideal N, Machado CM, Infante V, Braga DFO, Santos TG, Vidal C. Mechanical characterization and fatigue assessment of wire and arc additively manufactured HSLA steel parts. Int J Fatig 2022;164:107146. https://doi.org/10.1016/j.ijfatigue.2022.107146.
[19] Dinovitzer M, Chen X, Laliberte J, Huang X, Frei H. Effect of wire and arc additive manufacturing (WAAM) process parameters on bead geometry and microstructure. Addit Manuf 2019;26:138–46. https://doi.org/10.1016/j.addma.2018.12.013.
[20] Kumar V, Mandal A, Das AK, Kumar S. Parametric study and characterization of wire arc additive manufactured steel structures. Int J Adv Manuf Technol 2021;115:1723–33. https://doi.org/10.1007/s00170-021-07261-6.
[21] Panchenko O, Kladov I, Kurushkin D, Zhabrev L, Ryl'kov E, Zamozdra M. Effect of thermal history on microstructure evolution and mechanical properties in wire arc additive manufacturing of HSLA steel functionally graded components. Mater Sci Eng, A 2022;851:143569. https://doi.org/10.1016/j.msea.2022.143569.
[22] Yildiz AS, Davut K, Koc B, Yilmaz O. Wire arc additive manufacturing of high-strength low alloy steels: study of process parameters and their influence on the bead geometry and mechanical characteristics. Int J Adv Manuf Technol 2020;108:3391–404. https://doi.org/10.1007/s00170-020-05482-9.
[23] Norrish J, Polden J, Richardson I. A review of wire arc additive manufacturing: development, principles, process physics, implementation and current status. J Phys D Appl Phys 2021;54:473001. https://doi.org/10.1088/1361-6463/ac1e4a.
[24] Ban H, Shi G. A review of research on high-strength steel structures. Proc Inst Civ Eng - Struct Build 2018;171:625–41. https://doi.org/10.1680/jstbu.16.00197.
[25] Bhadeshia HKDH, Honeycombe RWK. Steels and properties. 2017.
[26] Hamelin CJ, Muránsky O, Smith MC, Holden TM, Luzin V, Bendeich PJ, et al. Validation of a numerical model used to predict phase distribution and residual stress in ferritic steel weldments. Acta Mater 2014;75:1–19. https://doi.org/10.1016/j.actamat.2014.04.045.
[27] Zhang Q, Xie J, Gao Z, London T, Griffiths D, Oancea V. A metallurgical phase transformation framework applied to SLM additive manufacturing processes. Mater Des 2019;166:107618. https://doi.org/10.1016/j.matdes.2019.107618.
[28] Kou S. Welding metallurgy. 2002. https://doi.org/10.1002/0471434027.
[29] Ouden G den, Hermans M. Welding Technology. 2009. Delft.
[30] Le VT, Mai DS, Hoang QH. Effects of cooling conditions on the shape, microstructures, and material properties of SS308L thin walls built by wire arc additive manufacturing. Mater Lett 2020;280:128580. https://doi.org/10.1016/j.matlet.2020.128580.
[31] Ge J, Lin J, Fu H, Lei Y, Xiao R. Tailoring microstructural features of wire arc additive manufacturing 2Cr13 part via varying inter-layer dwelling time. Mater Lett 2018;232:11–3. https://doi.org/10.1016/j.matlet.2018.08.037.
[32] Ding D, Wu B, Pan Z, Qiu Z, Li H. Wire arc additive manufacturing of Ti6AL4V using active interpass cooling. Mater Manuf Process 2020;35:845–51. https://doi.org/10.1080/10426914.2020.1732414.
[33] Mishra V, Babu A, Schreurs R, Wu K, Hermans MJM, Ayas C. Microstructure estimation and validation of ER110S-G steel structures produced by wire and arc additive manufacturing. J Mater Res Technol 2023. https://doi.org/10.1016/j.jmrt.2023.01.214.
[34] Rodrigues TA, Bairrão N, Farias FWC, Shamsolhodaei A, Shen J, Zhou N, et al. Steel-copper functionally graded material produced by twin-wire and arc additive manufacturing (T-WAAM). Mater Des 2022;213:110270. https://doi.org/10.1016/j.matdes.2021.110270.
[35] Suryakumar S, Karunakaran KP, Bernard A, Chandrasekhar U, Raghavender N, Sharma D. Weld bead modeling and process optimization in Hybrid Layered Manufacturing. CAD Comput Aided Des 2011;43:331–44. https://doi.org/10.1016/j.cad.2011.01.006.
[36] Palani PK, Murugan N. Selection of parameters of pulsed current gas metal arc welding. J Mater Process Technol 2006;172:1–10. https://doi.org/10.1016/j.jmatprotec.2005.07.013.
[37] Goldak J, Chakravarti A, Bibby M. A new finite element model for welding heat sources. Metall Trans B 1984;15:299–305. https://doi.org/10.1007/BF02667333.
[38] Peyre P, Dal M, Pouzet S, Castelnau O. Simplified numerical model for the laser metal deposition additive manufacturing process. J Laser Appl 2017;29:022304. https://doi.org/10.2351/1.4983251.

[39] De A, DebRoy T. A smart model to estimate effective thermal conductivity and viscosity in the weld pool. J Appl Phys 2004;95:5230–40. https://doi.org/10.1063/1.1695593.

[40] Ebrahimi A, Kleijn CR, Richardson IM. Numerical study of molten metal melt pool behaviour during conduction-mode laser spot melting. J Phys D Appl Phys 2020;54(10):105304. https://doi.org/10.1088/1361-6463/abca62.

[41] Goldak J, Bibby M, Moore J, House R, Patel B. Computer modeling of heat flow in welds. Metall Trans B 1986;17:587–600. https://doi.org/10.1007/BF02670226.

[42] Michaleris P. Modeling metal deposition in heat transfer analyses of additive manufacturing processes. Finite Elem Anal Des 2014;86:51–60. https://doi.org/10.1016/j.finel.2014.04.003.

[43] V E. The relationship between stress and strain for homogeneous deformation. J Inst Met 1948:537–62.

[44] Campbell JE, Thompson RP, Dean J, Clyne TW. Experimental and computational issues for automated extraction of plasticity parameters from spherical indentation. Mech Mater 2018;124:118–31. https://doi.org/10.1016/j.mechmat.2018.06.004.

[45] Campbell JE, Thompson RP, Dean J, Clyne TW. Comparison between stress-strain plots obtained from indentation plastometry, based on residual indent profiles, and from uniaxial testing. Acta Mater 2019;168:87–99. https://doi.org/10.1016/j.actamat.2019.02.006.

[46] Campbell JE, Gaiser-Porter M, Gu W, Ooi S, Burley M, Dean J, et al. Indentation plastometry of very hard metals. Adv Eng Mater 2022;24:2101398. https://doi.org/10.1002/adem.202101398.

[47] Gu W, Campbell J, Tang Y, Safaie H, Johnston R, Gu Y, et al. Indentation plastometry of welds. Adv Eng Mater 2022;24:2101645. https://doi.org/10.1002/adem.202101645.

[48] Clyne TW, Campbell JE, Burley M, Dean J. Profilometry-based inverse finite element method indentation plastometry. Adv Eng Mater 2021;23:2100437. https://doi.org/10.1002/adem.202100437.

[49] Van Der Wolk PJ, Wang J, Sietsma J, Van Der Zwaag S. Modelling the continuous cooling transformation diagram of engineering steels using neural networks Part I: phase regions. Zeitschrift Fuer Met Res Adv Tech 2002;93. https://doi.org/10.3139/146.021199.

[50] Thompson SW, Colvin DJ, Krauss G. Austenite decomposition during continuous cooling of an HSLA-80 plate steel. Metall Mater Trans A 1996;27:1557–71. https://doi.org/10.1007/BF02649815.

[51] Thompson SW, Vin Col DJ, Krauss G. Continuous cooling transformations and microstructures in a low-carbon, high-strength low-alloy plate steel. Metall Trans A 1990;21:1493–507. https://doi.org/10.1007/BF02672564.

[52] Palmeira Belotti L, van Dommelen JAW, Geers MGD, Goulas C, Ya W, Hoefnagels JPM. Microstructural characterisation of thick-walled wire arc additively manufactured stainless steel. J Mater Process Technol 2022;299:117373. https://doi.org/10.1016/j.jmatprotec.2021.117373.

[53] Donoghue J, Antonysamy AA, Martina F, Colegrove PA, Williams SW, Prangnell PB. The effectiveness of combining rolling deformation with Wire–Arc Additive Manufacture on β-grain refinement and texture modification in Ti–6Al–4V. Mater Char 2016;114:103–14. https://doi.org/10.1016/j.matchar.2016.02.001.

[54] Todaro CJ, Easton MA, Qiu D, Zhang D, Bermingham MJ, Lui EW, et al. Grain structure control during metal 3D printing by high-intensity ultrasound. Nat Commun 2020;11:142. https://doi.org/10.1038/s41467-019-13874-z.

[55] Wei HL, Mazumder J, DebRoy T. Evolution of solidification texture during additive manufacturing. Sci Rep 2015;5:16446. https://doi.org/10.1038/srep16446.

[56] Ghaffari M, Vahedi Nemani A, Rafieazad M, Nasiri A. Effect of solidification defects and HAZ softening on the anisotropic mechanical properties of a wire arc additive-manufactured low-carbon low-alloy steel part. Jom 2019;71:4215–24. https://doi.org/10.1007/s11837-019-03773-5.

[57] Babu SS. The mechanism of acicular ferrite in weld deposits. Curr Opin Solid State Mater Sci 2004;8. https://doi.org/10.1016/j.cossms.2004.10.001.

[58] Bourlet C, Zimmer-Chevret S, Pesci R, Bigot R, Robineau A, Scandella F. Microstructure and mechanical properties of high strength steel deposits obtained by Wire-Arc Additive Manufacturing. J Mater Process Technol 2020;285:116759. https://doi.org/10.1016/j.jmatprotec.2020.116759.

[59] Dirisu P, Ganguly S, Mehmanparast A, Martina F, Williams S. Analysis of fracture toughness properties of wire + arc additive manufactured high strength low alloy structural steel components. Mater Sci Eng, A 2019;765. https://doi.org/10.1016/j.msea.2019.138285.

[60] Katsumata M, Ishiyama O, Inoue T, Tanaka T. Microstructure and mechanical properties of bainite containing martensite and retained austenite in low carbon HSLA steels. Mater Trans, JIM 1991;32. https://doi.org/10.2320/matertrans1989.32.715.

[61] Rehan MA, Medvedeva A, Svensson L-E, Karlsson L. Retained austenite transformation during heat treatment of a 5 Wt pct Cr cold work tool steel. Metall Mater Trans A 2017;48:5233–43. https://doi.org/10.1007/s11661-017-4232-5.

[62] Mohammadijoo M, Valloton J, Collins L, Henein H, Ivey DG. Characterization of martensite-austenite constituents and micro-hardness in intercritical reheated and coarse-grained heat affected zones of API X70 HSLA steel. Mater Char 2018;142:321–31. https://doi.org/10.1016/j.matchar.2018.05.057.

[63] Lee S, Kim BC, Kwon D. Correlation of microstructure and fracture properties in weld heat- affected zones of thermomechanically controlled processed steels. Metall Trans A 1992;23:2803–16. https://doi.org/10.1007/BF02651759.

[64] Huda N, Midawi ARH, Gianetto J, Lazor R, Gerlich AP. Influence of martensite-austenite (MA) on impact toughness of X80 line pipe steels. Mater Sci Eng, A 2016;662:481–91. https://doi.org/10.1016/j.msea.2016.03.095.

[65] Davis CL, King JE. Effect of cooling rate on intercritically reheated microstructure and toughness in high strength low alloy steel. Mater Sci Technol 1993;9. https://doi.org/10.1179/mst.1993.9.1.8.

[66] Jorge JCF, Souza LFGD, Mendes MC, Bott IS, Araújo LS, Santos VRD, et al. Microstructure characterization and its relationship with impact toughness of C-Mn and high strength low alloy steel weld metals - a review. J Mater Res Technol 2021;10:471–501. https://doi.org/10.1016/j.jmrt.2020.12.006.

[67] Wang X, Shang C, Wang X. Characterization of the multi-pass weld metal and the effect of post-weld heat treatment on its microstructure and toughness. HSLA steels 2015, microalloying 2015 {\&} offshore eng. Steels 2015. Cham: Springer International Publishing; 2016. p. 481–8.

[68] Krauss G. Martensite in steel: strength and structure. Mater Sci Eng, A 1999;273–275:40–57. https://doi.org/10.1016/S0921-5093(99)00288-9.

[69] Krauss G. Tempering of lath martensite in low and medium carbon steels: assessment and challenges.

[70] Kim HJ, Kang BY. Effect of microstructural variation on weld metal cold cracking of HSLA-100 steel. ISIJ Int 2003;43:706–13. https://doi.org/10.2355/isijinternational.43.706.

[71] Kim K, Kang N, Kang M, Kim C. Assessment of heat-affected zone softening of hot-press-formed steel over 2.0 GPa tensile strength with bead-on-plate laser welding. Appl Sci 2021;11:5774. https://doi.org/10.3390/app11135774.

[72] López B, Rodriguez-Ibabe JM. Recrystallisation and grain growth in hot working of steels. Microstruct. Evol. Met. Form. Process.. Elsevier; 2012. p. 67–113. https://doi.org/10.1533/9780857096340.1.67.

[73] Hochhauser F, Ernst W, Rauch R, Vallant R, Enzinger N. Influence of the soft zone on the strength of welded modern hsla steels. Weld World 2012;56:77–85. https://doi.org/10.1007/BF03321352.

[74] Di X, Tong M, Li C, Zhao C, Wang D. Microstructural evolution and its influence on toughness in simulated inter-critical heat affected zone of large thickness bainitic steel. Mater Sci Eng, A 2019;743:67–76. https://doi.org/10.1016/j.msea.2018.11.070.

[75] Zhang P, Li SX, Zhang ZF. General relationship between strength and hardness. Mater Sci Eng, A 2011;529:62–73. https://doi.org/10.1016/j.msea.2011.08.061.